

# High-resolution crystal structure of the human CB1 cannabinoid receptor

Zhenhua Shao<sup>1</sup>, Jie Yin<sup>1</sup>, Karen Chapman<sup>1</sup>, Magdalena Grzemska<sup>1</sup>, Lindsay Clark<sup>1</sup>, Junmei Wang<sup>2</sup> & Daniel M. Rosenbaum<sup>1</sup>

**The human cannabinoid G-protein-coupled receptors (GPCRs) CB1 and CB2 mediate the functional responses to the endocannabinoids anandamide and 2-arachidonyl glycerol (2-AG) and to the widely consumed plant phytocannabinoid  $\Delta^9$ -tetrahydrocannabinol (THC)<sup>1</sup>. The cannabinoid receptors have been the targets of intensive drug discovery efforts, because modulation of these receptors has therapeutic potential to control pain<sup>2</sup>, epilepsy<sup>3</sup>, obesity<sup>4</sup>, and other disorders. Although much progress in understanding the biophysical properties of GPCRs has recently been made, investigations of the molecular mechanisms of the cannabinoids and their receptors have lacked high-resolution structural data. Here we report the use of GPCR engineering and lipidic cubic phase crystallization to determine the structure of the human CB1 receptor bound to the inhibitor taranabant at 2.6-Å resolution. We found that the extracellular surface of CB1, including the highly conserved membrane-proximal N-terminal region, is distinct from those of other lipid-activated GPCRs, forming a critical part of the ligand-binding pocket. Docking studies further demonstrate how this same pocket may accommodate the cannabinoid agonist THC. Our CB1 structure provides an atomic framework for studying cannabinoid receptor function and will aid the design and optimization of therapeutic modulators of the endocannabinoid system.**

The endocannabinoid signalling system in mammals comprises endogenous lipid messengers (anandamide and 2-AG) and two homologous GPCRs (CB1, which is located in the nervous system and periphery, and CB2, which is expressed primarily in immune cells)<sup>1</sup>. Human CB1 and CB2 (which share 42% sequence identity) are also activated by natural products<sup>5</sup> such as THC and by synthetic cannabinoids and can be inhibited by diverse subtype-selective and non-selective antagonists and inverse agonists<sup>6</sup>. CB1 is the most abundant GPCR in the central nervous system (CNS) and regulates diverse brain functions and behaviours, modulating neurotransmitter release and neuronal excitation through the pre-synaptic activation of the G-protein  $G_{i/o}$  (inhibiting adenylyl cyclase), GIRK channels, and arrestin/MAP kinase signalling<sup>7</sup>. Endocannabinoids are synthesized postsynaptically by lipases and travel across synapses in a retrograde manner<sup>8</sup>, embedding in the presynaptic membrane where they can activate CB1<sup>9</sup>. Beyond the CNS, CB1 signalling in peripheral tissues has been implicated in other physiological mechanisms such as release of the metabolic hormones leptin and insulin<sup>10,11</sup>. However, the mechanism by which lipidic or lipophilic cannabinoid agonists access their GPCR-binding sites and promote receptor activation through specific binding interactions is, as yet, unknown.

Although humans have been consuming phytocannabinoids for their psychotropic effects for thousands of years<sup>1</sup>, THC was only found to be the active chemical constituent of *Cannabis sativa* in 1964 (ref. 12). Recently, alternative therapeutic uses for cannabinoid ligands have been pursued. As the endocannabinoid system is involved in the regulation of energy metabolism<sup>4</sup>, synthetic inverse agonists such as rimonabant and

taranabant have proven effective in the clinic for treatment of obesity, but have failed to secure regulatory approval owing to adverse CNS side effects<sup>13</sup>. Peripheral blockade of CB1 by non-penetrant inverse agonists may represent an alternative therapeutic strategy for treating obesity, while avoiding CB1 receptors in the CNS<sup>10</sup>. Natural and synthetic cannabinoid ligands have also shown considerable promise in the treatment of neuropathic pain<sup>2</sup> and epilepsy-induced seizures<sup>3</sup>. To gain further insight into the molecular mechanisms of cannabinoid system modulators and aid structure-based ligand design, we sought to crystallize the human CB1 receptor and solve its atomic structure.

Obtaining diffraction-quality crystals of CB1 required optimization of both the construct and the purification technique. We carried out differential scanning fluorimetry on the detergent-solubilized receptor, which identified the inverse agonist taranabant as a ligand conferring enhanced thermostability (Methods and Extended Data Fig. 1). To promote lipidic cubic phase (LCP) crystallization, we replaced the third intracellular loop (ICL3) of CB1 with the thermostable PGS (*Pyrococcus abyssi* glycogen synthase) domain, which recently proved essential in helping solve crystal structures of the human orexin receptors<sup>14</sup>. We also incorporated the point mutation T210A, which was previously shown to stabilize the inactive conformation of CB1 and increase thermostability<sup>15</sup>. Finally, we truncated CB1(T210A)-PGS by eliminating the first 89 N-terminal residues and the C terminus after residue 421. The engineered construct binds to the inverse agonists taranabant and

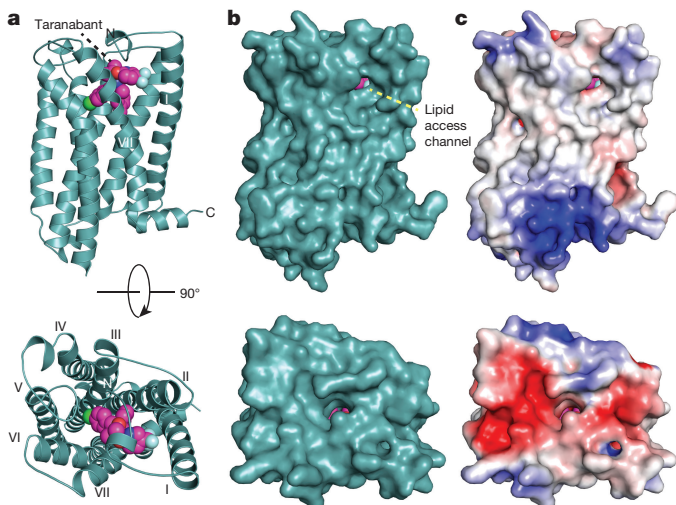


**Figure 1 | Global structure of CB1 bound to taranabant.** **a**, CB1 is represented as a teal cartoon. The taranabant ligand is shown as spheres with magenta carbon atoms. Views are from within the plane of the membrane (top) and from the extracellular space (bottom). **b**, Solvent-accessible surface representation of CB1 from the same views as in **a**. **c**, CB1 surface representation coloured according to electrostatic potential, from red (negative) to blue (positive).

<sup>1</sup>Department of Biophysics, The University of Texas Southwestern Medical Center, Dallas, Texas 75390, USA. <sup>2</sup>Green Center for Systems Biology, The University of Texas Southwestern Medical Center, Dallas, Texas 75390, USA.

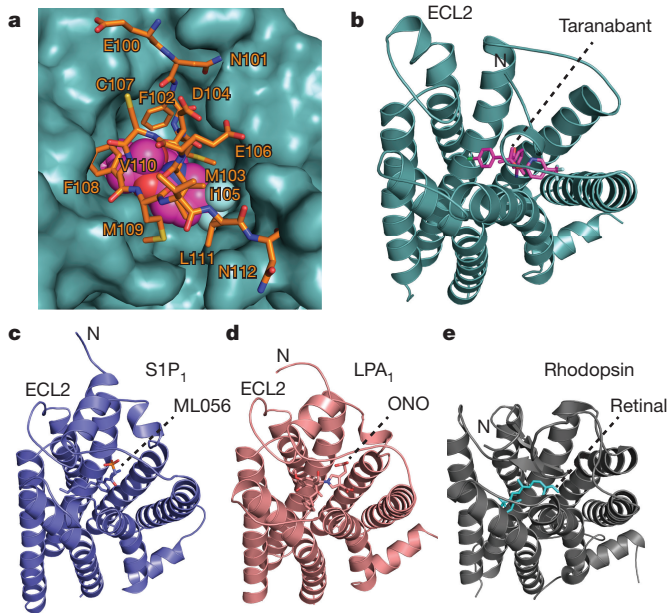


**Figure 2 | Membrane-proximal N-terminal region of CB1.** **a**, Interaction between the membrane-proximal N-terminal region and the rest of the receptor. Residues 100–112 are shown as orange sticks, and taranabant is shown as magenta spheres. The remainder of CB1 is depicted as a teal solvent-accessible surface. **b**, The extracellular region of CB1, with the receptor as a teal cartoon and taranabant as magenta sticks. **c**, The S1P<sub>1</sub> receptor (PDB accession number 3V2Y) is depicted as a blue cartoon, from the same perspective as in **a** after superposition with CB1. The ML056 antagonist is shown as blue sticks. **d**, The LPA<sub>1</sub> receptor (PDB accession number 4Z35) as a salmon cartoon, from the same perspective as in **a** after superposition with CB1. The ONO 9910539 antagonist is shown as salmon sticks. **e**, The GPCR rhodopsin (PDB accession number 1F88) as a grey cartoon, from the same perspective as in **a** after superposition with CB1. The 11-*cis*-retinal inverse agonist ligand is shown as cyan sticks. Glycosyl moieties in the N-terminal region are removed for clarity.

rimonabant (also denoted SR141716A) in a manner nearly identical to wild-type CB1. CB1(T210A)-PGS has, however, a sevenfold lower affinity for the agonist CP55940, consistent with stabilization of an inactive conformation (Extended Data Fig. 2) and in agreement with the original report of the T210A mutation<sup>15</sup>. After purifying this construct from Sf9 insect cells (Methods and Extended Data Fig. 3), we obtained LCP microcrystals that diffracted to 2.6 Å resolution, solved the structure by molecular replacement and refined the structure to an *R*<sub>free</sub> value of 0.23 (Methods and Extended Data Table 1). In the monoclinic crystals, CB1(T210A)-PGS packs in a manner such that the extracellular-facing ligand-binding region is not involved in lattice contacts (Extended Data Fig. 4a), and the receptor and ligand are well ordered with low overall *B* factors. Although truncation of the N terminus of CB1 was necessary to form diffraction-quality crystals, such modifications may affect the functional properties of the receptor, as indicated by the variable expression and pharmacology of tissue-specific splice variants in this region<sup>16</sup>. Nevertheless, our binding data (Extended Data Fig. 2) and previous precedent<sup>17</sup> show that the basic inverse-agonist-and agonist-binding properties of CB1 are maintained in a receptor lacking the N-terminal 89 residues (which also contains three consensus N-linked glycosylation motifs).

The global structure of the CB1 receptor, with its classical seven-transmembrane fold, is shown in Fig. 1. Using other rhodopsin family (class A) GPCRs as guides<sup>18</sup>, the taranabant-bound CB1 structure represents an inactive conformation with respect to G-protein binding, with a canonical ionic lock formed between Arg214<sup>3,50</sup> and Asp338<sup>6,30</sup> (distance, 3.4 Å; Ballesteros–Weinstein numbering used in superscript). At the extracellular surface, the second extracellular loop (ECL2) and

the membrane-proximal N-terminal region preceding transmembrane domain 1 (TM1) form a lid over the orthosteric pocket, which almost completely shields taranabant from the solvent (Fig. 1a, b). As is observed in the structure of the lipid-activated GPCR S1P<sub>1</sub> (ref. 19), a gap between TM1 and TM7 in the extracellular leaflet (Fig. 1b) may contribute to a membrane-embedded access channel for lipophilic agonists. Further dilation of the highly conserved residues (Ile119<sup>1,35</sup>, Phe381<sup>7,37</sup>, and Met384<sup>7,40</sup>) that line this channel (Extended Data Fig. 5) would be required to facilitate entry of ligands. Previous molecular dynamics proposed that the endocannabinoid 2-AG enters into the homologous CB2 receptor between TM6 and TM7 (ref. 20); however, these two transmembrane domains are tightly associated in the present structure. Taranabant makes multiple contacts with both TM1 and TM7 and fills the orthosteric pocket directly inside the TM1–TM7 opening, potentially acting as a plug that blocks entry of the endocannabinoid. The extracellular face and lid above the orthosteric pocket contain an abundance of acidic residues, giving a negatively charged surface that will energetically disfavour interaction with negatively charged ligands (Fig. 1c). This feature of CB1 may help to ensure lipid-binding selectivity in a bilayer containing a high concentration of negatively charged phospholipids.

The first part of the N terminus of CB1 observed in the electron density of our crystals begins at E100. The 13 membrane-proximal amino acids that precede TM1 fold over the ligand-binding pocket and interact with TM2, TM3, ECL2, and TM7 (Fig. 2a, b). This region is highly conserved in CB1 (Extended Data Fig. 6) and contributes extensively to interaction with taranabant (as will be discussed). The occluded nature of the CB1 orthosteric pocket was predicted by a study showing that disulfide bond formation between Cys98 and Cys107 modulates orthosteric ligand binding<sup>21</sup>; however, this disulfide bond is either not present or not visible in the current structure (possibly owing to cysteine capping by iodoacetamide). To assess the flexibility of the N-terminal region of CB1, we carried out a 60-ns molecular dynamics simulation of the CB1 structure embedded in an explicit POPC bilayer in the presence and absence of taranabant. In both cases, the N-terminal region was highly stable over the course of the simulation, exhibiting low root mean squared deviation (r.m.s.d.) values comparable to those of the entire transmembrane bundle (Extended Data Fig. 7). These results support the idea that the N-terminal region of CB1 will maintain a conformation similar to the structure observed here, even in the absence of ligand. Other lipid-activated GPCRs that have been structurally characterized (S1P<sub>1</sub> and LPA<sub>1</sub>; refs 19 and 22, respectively) contain a disulfide-cross-linked ECL2 structure that is very similar to that of CB1; however, the N-terminal regions of these receptors are markedly different, containing  $\alpha$ -helices that sit above the membrane and pack between ECL1 and ECL2 (Fig. 2c, d). The occluded orthosteric pocket of CB1, with the N-terminal region folding over the buried hydrophobic inverse agonist taranabant, is mirrored in the structure of the visual photoreceptor rhodopsin bound to 11-*cis*-retinal<sup>23</sup> (Fig. 2e). A gap between TM1 and TM7 was proposed as part of a channel for uptake and release of the lipophilic 11-*cis*-retinal ligand, based on the structure of the ligand-free opsin in an active conformation<sup>24</sup>, further paralleling the structure of CB1. The opsin residues Leu40<sup>1,35</sup>, Ile290<sup>7,37</sup>, and Phe293<sup>7,40</sup> surrounding this gap are analogous to CB1 residues Ile119<sup>1,35</sup>, Phe381<sup>7,37</sup>, and Met384<sup>7,40</sup> (Extended Data Fig. 5).

Taranabant is a subtype-selective inverse agonist with an inhibition constant (*K*<sub>i</sub>) of 0.13 nM for CB1 and a *K*<sub>i</sub> of 170 nM for CB2 (ref. 25). Unambiguous electron density at the orthosteric ligand-binding pocket (Extended Data Fig. 4b, c) placed taranabant at an unusual site, towards TM1 and TM7, contrasting with the space occupied by inhibitors of other class A GPCRs, such as the  $\beta_2$  adrenergic receptor<sup>18</sup> (Fig. 3a). Taranabant adopts a conformation in which the chlorophenyl moiety extends towards TM5, the cyanophenyl buries deeper into the seven transmembrane bundle and the trifluoromethylpyridine projects into the putative access channel between TM1 and TM7 (Fig. 3b).

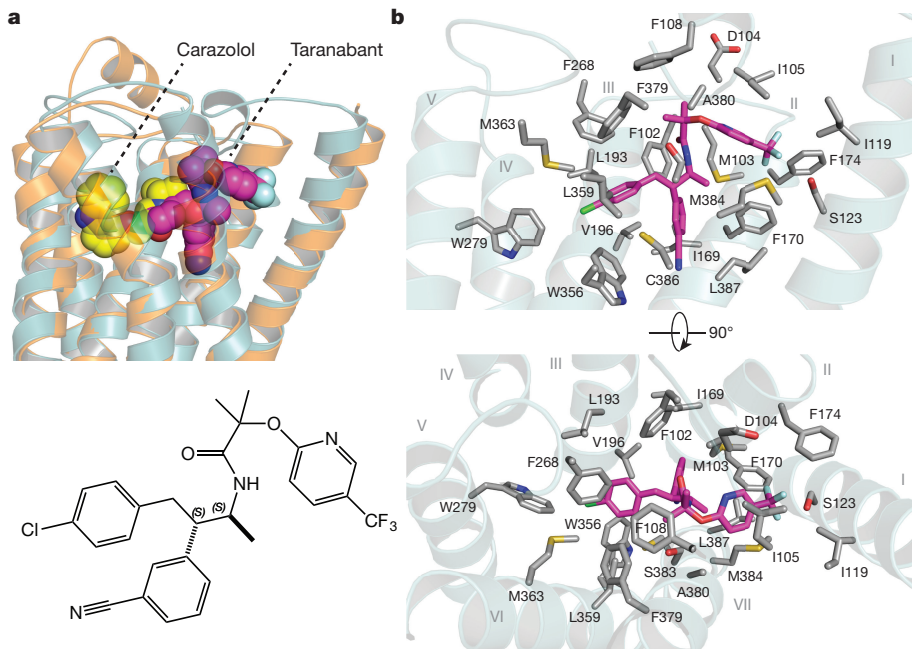


**Figure 3 | Binding of taranabant to the CB1 receptor.** **a**, Cartoon of CB1 (translucent, teal) with a cartoon of  $\beta_2$ AR (PDB accession number 2RH1; translucent, orange) superimposed. The r.m.s.d. for the  $C\alpha$  positions is 2.6 Å. The beta blocker carazolol is represented by yellow spheres, taranabant by magenta spheres. At the bottom is a 2D representation

of taranabant. **b**, Contact residues with 4 Å of taranabant in the CB1 structure. The receptor side chains are shown as grey sticks, the backbone is a transparent cartoon and taranabant is in magenta. Top view is from within the plane of the bilayer (TM6 and TM7 cartoons removed for clarity), bottom view is from the extracellular space.

The orthosteric binding pocket of CB1 is highly hydrophobic, as is expected for a lipid-activated receptor. Of the 24 residues within 4 Å of the ligand, there are only three polar side chains: Asp104, whose acidic side chain points towards the extracellular space; Ser123<sup>1,39</sup> near the access channel that forms a polar contact with the trifluoromethyl group of taranabant; and Ser383<sup>7,39</sup>, which has been implicated in agonist binding<sup>26</sup>. By contrast, a large number of hydrophobic residues (including six Phe, three Met, two Trp, three Leu, and three Ile side chains) line the orthosteric pocket and make a variety of hydrophobic contacts with taranabant, burying 1,109 Å<sup>2</sup> of surface area (Fig. 3b). All of the taranabant contact residues on CB1 are absolutely conserved across the vertebrate lineage, with the exception of Ile105, which can be replaced by Met (Extended Data Fig. 8). The major divergence between CB1 and CB2 within the subset of binding residues lies in the membrane-proximal N-terminal region, where Phe102, Met103, Asp104, Ile105, and Phe108 make van der Waals contacts with taranabant. The subtype selectivity of taranabant for CB1 may arise from the divergence of this region between CB1 and CB2.

Taranabant (Fig. 3a) and rimonabant (Fig. 4a) have related chemical structures and similar conformational properties in isolation<sup>27</sup>. Docking of rimonabant with the CB1 crystal structure yielded a low-energy pose that overlaps almost completely with that of taranabant, contacting the same constellation of residues (Fig. 4a). This supports the use of the current structure to analyse the binding modes of both ligands. Mutagenesis studies have identified several residues whose mutation caused a loss in taranabant and/or rimonabant binding affinity<sup>27–30</sup>. Indeed, many of these residues are in contact with the ligand in the CB1 structure, including Phe170<sup>2,57</sup>, Phe174<sup>2,61</sup>, Leu193<sup>3,29</sup>, Trp279<sup>5,43</sup>, Trp356<sup>6,48</sup>, Phe379<sup>7,35</sup>, and Leu387<sup>7,42</sup>. However, several residues on TM3 and TM5 (for example, Lys192<sup>3,28</sup>, Phe200<sup>3,36</sup>, and Tyr275<sup>5,39</sup>) are not within contact distance of taranabant and appear to make indirect contributions to binding, through structural stabilization or influence of the conformational equilibrium of CB1.

To gain insight into the initial recognition of agonists by the CB1 receptor, we docked THC (a partial agonist<sup>5</sup>) into our crystal structure coordinates using the program Glide (see Methods). The top docking

poses have the tricyclic core of THC binding between TM1, TM2 and TM7 (as with taranabant), with the C3 alkyl chain overlapping with the chlorophenyl moiety of taranabant and extending towards Trp356<sup>6,48</sup> (Fig. 4b). Conformational changes in this residue and its surroundings have been proposed as a trigger for CB1 activation, and mutation to alanine leads to enhanced stimulation ( $E_{max}$ ) by CB1 agonists<sup>31</sup>. Previous mutagenesis experiments have also identified Phe174<sup>2,61</sup>, Leu193<sup>3,29</sup>, and Ser383<sup>7,39</sup> as important residues for binding of THC or related agonists such as CP55940 (refs 26, 32). These residues are either in contact with or in close proximity to the preferred docking pose of THC. One caveat to these calculations is that the inactive structure of CB1 is not ideal for predicting high-affinity agonist interactions. It should, however, be noted that the crystallization construct (stabilized in an inactive conformation) still displays significant affinity for CP55940 (Extended Data Fig. 2). Finally, Cys355<sup>6,47</sup> on the bilayer-facing side of TM6 was reported to form a covalent adduct with a THC analogue that possesses a reactive group at the end of the C3-pentyl chain<sup>33</sup>. Starting with our THC pose, such cross-linking would require rotation of TM6 at the orthosteric pocket during CB1 activation and consequent disruption of the packing around Trp356<sup>6,48</sup>.

While our manuscript was under review, a crystal structure of human CB1 was reported<sup>34</sup> bound to the antagonist AM6538, which closely resembles rimonabant but has a nitrate group substituted on ‘arm 2’ of the rimonabant core (that is, the chlorophenyl moiety in Fig. 4a). Although the taranabant-bound crystal structure reported here and the AM6538-bound structure are in general agreement (Extended Data Fig. 9a), there are several differences that may be important for functional interpretation and prediction. Notably, the electron density for the ligand and the important N-terminal region is weak in the AM6538-bound structure, with high  $B$  factors in the refined model (average  $B = 134.3 \text{ \AA}^2$  for residues 99–112 and  $B = 119.5 \text{ \AA}^2$  for the ligand). By contrast, the equivalent region in our taranabant-bound structure is very well ordered, with good density and much lower  $B$  factors (average  $B = 61.7 \text{ \AA}^2$  for residues 100–112 and  $B = 42.0 \text{ \AA}^2$  for the ligand) (Extended Data Fig. 9b, c). The lack of clear density and resulting model ambiguity for the N-terminal region in the AM6538-bound structure

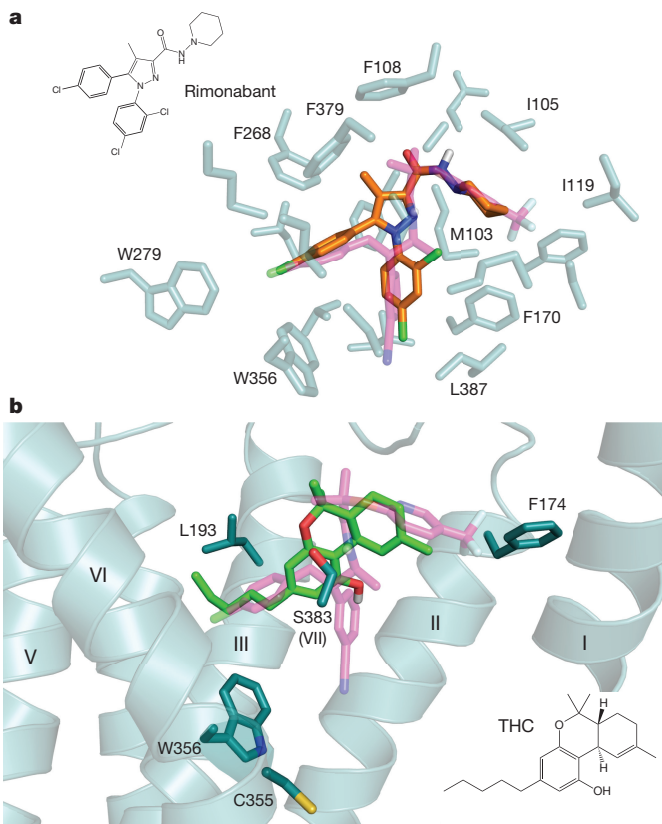


**Figure 4 | Docking of rimonabant and THC to the CB1 receptor.**

a, Overlay of the crystal structure pose of taranabant (transparent magenta sticks) with the top-scoring docking pose of rimonabant shown using orange sticks (see Methods). The contact residues within 4 Å of taranabant are shown as transparent teal sticks. The 2D structure of rimonabant is shown at upper left. b, Top-scoring docking pose of THC is shown as light green sticks, along with taranabant (transparent magenta sticks). Selected residues important for the binding of THC and agonist activity are shown as teal sticks. TM7 cartoon is removed for clarity. The 2D structure of THC is shown on the bottom right.

may limit its utility for predicting the binding modes of other ligands. This is apparent in the erroneous docking prediction for taranabant, in which arm 1 and arm 2 (chlorophenyl and cyanophenyl groups) are swapped relative to their experimentally determined binding positions reported herein. Further biochemical and computational studies will be required to establish the relative utility of these two crystal structures as templates for ligand docking and design.

GPCRs adopt multiple conformations, creating a complex energy landscape that allows the binding of different ligands to modulate different intracellular effectors, such as G proteins and arrestin<sup>35</sup>. CB1 has considerable agonist-independent constitutive activity<sup>36</sup> and exhibits subtle and paradoxical pharmacological properties; it is antagonized by cannabidiol (a molecule that, but for a bond disconnection, is near-identical to THC)<sup>5</sup> and inhibited by the compound ORG27569, which allosterically increases agonist affinity but decreases subsequent receptor activation<sup>37</sup>. Understanding these phenomena will require additional structures of CB1 in different conformational states, bound to a range of ligands (both orthosteric and allosteric) of differing efficacy. Our structure of CB1 bound to taranabant represents a step in this direction and provides a crystallographic basis for computational design of cannabinoid system modulators.

**Online Content** Methods, along with any additional Extended Data display items and Source Data, are available in the online version of the paper; references unique to these sections appear only in the online paper.

Received 6 October; accepted 8 November 2016.

Published online 16 November 2016.

- Mechoulam, R. & Parker, L. A. The endocannabinoid system and the brain. *Annu. Rev. Psychol.* **64**, 21–47 (2013).
- Lynch, M. E. & Ware, M. A. Cannabinoids for the treatment of chronic non-cancer pain: an updated systematic review of randomized controlled trials. *J. Neuroimmune Pharmacol.* **10**, 293–301 (2015).
- Reddy, D. S. & Golub, V. M. The pharmacological basis of cannabis therapy for epilepsy. *J. Pharmacol. Exp. Ther.* **357**, 45–55 (2016).
- Kim, J., Li, Y. & Watkins, B. A. Endocannabinoid signaling and energy metabolism: a target for dietary intervention. *Nutrition* **27**, 624–632 (2011).
- Pertwee, R. G. The diverse CB1 and CB2 receptor pharmacology of three plant cannabinoids: Δ9-tetrahydrocannabinol, cannabidiol and Δ9-tetrahydrocannabivarin. *Br. J. Pharmacol.* **153**, 199–215 (2008).
- Vemuri, V. K. & Makriyannis, A. Medicinal chemistry of cannabinoids. *Clin. Pharmacol. Ther.* **97**, 553–558 (2015).
- Howlett, A. C. et al. Cannabinoid physiology and pharmacology: 30 years of progress. *Neuropharmacology* **47** (Suppl. 1), 345–358 (2004).
- Wilson, R. I. & Nicoll, R. A. Endocannabinoid signaling in the brain. *Science* **296**, 678–682 (2002).
- Fowler, C. J. Transport of endocannabinoids across the plasma membrane and within the cell. *FEBS J.* **280**, 1895–1904 (2013).
- Tam, J. et al. Peripheral cannabinoid-1 receptor inverse agonism reduces obesity by reversing leptin resistance. *Cell Metab.* **16**, 167–179 (2012).
- Jourdan, T. et al. Activation of the Nlrp3 inflammasome in infiltrating macrophages by endocannabinoids mediates beta cell loss in type 2 diabetes. *Nat. Med.* **19**, 1132–1140 (2013).
- Gaoni, Y. & Mechoulam, R. Isolation, structure, and partial synthesis of an active constituent of hashish. *J. Am. Chem. Soc.* **86**, 1646–1647 (1964).
- Janero, D. R. & Makriyannis, A. Cannabinoid receptor antagonists: pharmacological opportunities, clinical experience, and translational prognosis. *Expert Opin. Emerg. Drugs* **14**, 43–65 (2009).
- Yin, J. et al. Structure and ligand-binding mechanism of the human OX1 and OX2 orexin receptors. *Nat. Struct. Mol. Biol.* **23**, 293–299 (2016).
- D'Antona, A. M., Ahn, K. H. & Kendall, D. A. Mutations of CB1 T210 produce active and inactive receptor forms: correlations with ligand affinity, receptor stability, and cellular localization. *Biochemistry* **45**, 5606–5617 (2006).
- González-Mariscal, I. et al. Human CB1 receptor isoforms, present in hepatocytes and β-cells, are involved in regulating metabolism. *Sci. Rep.* **6**, 33302 (2016).
- Andersson, H., D'Antona, A. M., Kendall, D. A., Von Heijne, G. & Chin, C. N. Membrane assembly of the cannabinoid receptor 1: impact of a long N-terminal tail. *Mol. Pharmacol.* **64**, 570–577 (2003).
- Rosenbaum, D. M. et al. GPCR engineering yields high-resolution structural insights into β2-adrenergic receptor function. *Science* **318**, 1266–1273 (2007).
- Hanson, M. A. et al. Crystal structure of a lipid G protein-coupled receptor. *Science* **335**, 851–855 (2012).
- Hurst, D. P. et al. A lipid pathway for ligand binding is necessary for a cannabinoid G protein-coupled receptor. *J. Biol. Chem.* **285**, 17954–17964 (2010).
- Fay, J. F. & Farrens, D. L. The membrane proximal region of the cannabinoid receptor CB1 N-terminus can allosterically modulate ligand affinity. *Biochemistry* **52**, 8286–8294 (2013).
- Chrencik, J. E. et al. Crystal structure of antagonist bound human lysophosphatidic acid receptor 1. *Cell* **161**, 1633–1643 (2015).
- Palczewski, K. et al. Crystal structure of rhodopsin: A G protein-coupled receptor. *Science* **289**, 739–745 (2000).
- Park, J. H., Scheerer, P., Hofmann, K. P., Choe, H.-W. & Ernst, O. P. Crystal structure of the ligand-free G-protein-coupled receptor opsin. *Nature* **454**, 183–187 (2008).
- Fong, T. M. et al. Antisobesity efficacy of a novel cannabinoid-1 receptor inverse agonist, N-[1(S,2S)-3-(4-chlorophenyl)-2-(3-cyanophenyl)-1-methylpropyl]-2-methyl-2-[5-(trifluoromethyl)pyridin-2-yl]oxypropanamide (MK-0364), in rodents. *J. Pharmacol. Exp. Ther.* **321**, 1013–1022 (2007).
- Kapur, A. et al. Mutation studies of Ser7.39 and Ser2.60 in the human CB1 cannabinoid receptor: evidence for a serine-induced bend in CB1 transmembrane helix 7. *Mol. Pharmacol.* **71**, 1512–1524 (2007).
- Lin, L. S. et al. Conformational analysis and receptor docking of N-[1(S,2S)-3-(4-chlorophenyl)-2-(3-cyanophenyl)-1-methylpropyl]-2-methyl-2-[5-(trifluoromethyl)pyridin-2-yl]oxypropanamide (taranabant, MK-0364), a novel, acyclic cannabinoid-1 receptor inverse agonist. *J. Med. Chem.* **51**, 2108–2114 (2008).
- Shim, J.-Y., Bertalovitz, A. C. & Kendall, D. A. Probing the interaction of SR141716A with the CB1 receptor. *J. Biol. Chem.* **287**, 38741–38754 (2012).
- Sitkov, D. F. et al. Cannabinoid CB(1) receptor ligand binding and function examined through mutagenesis studies of F200 and S383. *Eur. J. Pharmacol.* **651**, 9–17 (2011).

30. Hurst, D. P. et al. *N*-(piperidin-1-yl)-5-(4-chlorophenyl)-1-(2,4-dichlorophenyl)-4-methyl-1H-pyrazole-3-carboxamide (SR141716A) interaction with LYS 3.28(192) is crucial for its inverse agonism at the cannabinoid CB1 receptor. *Mol. Pharmacol.* **62**, 1274–1287 (2002).
31. McAllister, S. D. et al. Structural mimicry in class A G protein-coupled receptor rotamer toggle switches: the importance of the F3.36(201)/W6.48(357) interaction in cannabinoid CB1 receptor activation. *J. Biol. Chem.* **279**, 48024–48037 (2004).
32. Shim, J.-Y., Bertalovitz, A. C. & Kendall, D. A. Identification of essential cannabinoid-binding domains: structural insights into early dynamic events in receptor activation. *J. Biol. Chem.* **286**, 33422–33435 (2011).
33. Picone, R. P. et al. (−)-7-Isothiocyanato-11-hydroxy-1,1'-dimethylheptylhexahydrodrcannabinol (AM841), a high-affinity electrophilic ligand, interacts covalently with a cysteine in helix six and activates the CB1 cannabinoid receptor. *Mol. Pharmacol.* **68**, 1623–1635 (2005).
34. Hua, T. et al. Crystal structure of the human cannabinoid receptor CB1. *Cell* **167**, 750–762.e14 (2016).
35. Manglik, A. et al. Structural insights into the dynamic process of β2-adrenergic receptor signaling. *Cell* **161**, 1101–1111 (2015).
36. Console-Bram, L., Marcu, J. & Abood, M. E. Cannabinoid receptors: nomenclature and pharmacological principles. *Prog. Neuropsychopharmacol. Biol. Psychiatry* **38**, 4–15 (2012).
37. Price, M. R. et al. Allosteric modulation of the cannabinoid CB1 receptor. *Mol. Pharmacol.* **68**, 1484–1495 (2005).

**Acknowledgements** We thank the staff of the GM/CA-CAT beamline 23ID at the Advanced Photon Source (APS) for support during data collection. This project was supported by Welch Foundation grant (I-1770 to D.M.R) and a Packard Foundation Fellowship (D.M.R.). APS is a US Department of Energy Office of Science User Facility operated for the DOE Office of Science by Argonne National Laboratory (DE-AC02-06CH11357).

**Author Contributions** Z.S. developed the CB1 construct and purification; expressed, purified and crystallized the receptor; collected diffraction data; and solved and refined the structure. J.Y. assisted with crystallographic refinement. K.C. performed ligand binding assays on CB1 constructs. M.G. carried out computational docking calculations. L.C. assisted with construct design and purification. J.W. performed and supervised computational docking calculations and molecular dynamics simulations. D.M.R supervised the overall project, assisted with collection of diffraction data, and wrote the manuscript.

**Author Information** Reprints and permissions information is available at [www.nature.com/reprints](http://www.nature.com/reprints). The authors declare no competing financial interests. Readers are welcome to comment on the online version of the paper. Correspondence and requests for materials should be addressed to D.M.R. (dan.rosenbaum@utsouthwestern.edu).

**Reviewer Information** *Nature* thanks A. Christopoulos, G. Kunos and the other anonymous reviewer(s) for their contribution to the peer review of this work.

## METHODS

**Cloning, expression and purification.** The wild-type human CB1 receptor gene (Uniprot Entry: P21554) was cloned into a modified pFastBac (Invitrogen) baculovirus expression vector with the haemagglutinin (HA) signal sequence followed by a Flag epitope tag at the N terminus and a 10× His-tag at the C terminus. To facilitate receptor crystallization, the 76 N-terminal residues were removed, a TEV protease recognition site was introduced before residue Lys90, and the 51 C-terminal residues were deleted (truncation after Pro421). Residues 302–332 in the CB1 intracellular loop 3 (ICL3) were replaced with a synthetic DNA fragment containing the 196-amino acid coding sequence of *P. abyssi* glycogen synthase (PDB accession number: 2FBW). Finally, the mutation T210A was introduced by an adapted Multi-site Quickchange protocol (Stratagene).

The final CB1(T210A)–PGS fusion construct was transfected into DH10Bac to produce a recombinant baculovirus with the Bac-to-Bac system (Invitrogen). The recombinant baculovirus was used to infect Sf9 insect cell culture at a cell density of  $2.5 \times 10^6$  cells per ml<sup>-1</sup>, with 1 μM taranabant (Tocris) added to the medium. Infected cells were grown for 60 h at 27 °C before harvesting, and the cell pellets were stored at –80 °C for future use.

Sf9 cell membranes were disrupted by thawing frozen cell pellets in a hypotonic buffer containing 10 mM Tris pH 7.5, 1 mM EDTA, 160 μg ml<sup>-1</sup> benzamidine, 100 μg ml<sup>-1</sup> leupeptin, 2 mg ml<sup>-1</sup> iodoacetamide and 1 μM taranabant. The cell membranes were centrifuged at 10,000 g for 20 min at 4 °C. Membrane pellets were solubilized in a buffer containing 50 mM HEPES, pH 7.5, 500 mM NaCl, 1% (w/v) *n*-dodecyl β-D-maltopyranoside (DDM; Anatrace), 0.2% sodium cholate, 0.2% cholesteryl hemi-succinate (CHS), 10% glycerol, 160 μg ml<sup>-1</sup> benzamidine, 100 μg ml<sup>-1</sup> leupeptin, 2 mg ml<sup>-1</sup> iodoacetamide and 10 μM taranabant for 1 h at 4 °C. The supernatant was isolated after ultra-centrifugation for 30 min at 100,000 g and incubated with Ni-NTA agarose beads (GE Healthcare) in batch for 3 h at 4 °C. After binding, the beads were collected by centrifugation at 100 g and washed with five volumes of Ni-NTA wash buffer (50 mM HEPES, pH 7.5, 500 mM NaCl, 0.05% (w/v) DDM, 0.01% sodium cholate, 0.01% CHS, 10% glycerol, 50 mM imidazole, 160 μg ml<sup>-1</sup> benzamidine, 100 μg ml<sup>-1</sup> leupeptin and 1 μM taranabant). After transfer to a gravity column, beads were washed with 15 column volumes of Ni-NTA wash buffer, and receptor protein was eluted in Ni-NTA wash buffer with 200 mM imidazole and 2 mM calcium. The eluted protein was then loaded by gravity flow over anti-Flag M1 affinity resin. Detergent was exchanged from 0.05% DDM to 0.05% lauryl maltose neopentyl glycol (LMNG) on the M1 resin. Finally the pure receptor was eluted with 0.2 mg ml<sup>-1</sup> Flag peptide and 5 mM EDTA. TEV protease (1:10 w/w) and PNGase F were added to the eluate, and protein was incubated at 4 °C overnight. Finally, the receptor was run on a Superdex 200 size-exclusion column (GE Healthcare) with buffer containing 20 mM HEPES, pH 7.5, 150 mM NaCl, 0.05% LMNG, and 1 μM taranabant.

**Differential scanning fluorimetry.** Protein samples were purified and prepared in the absence of ligand (apo), with taranabant, or with rimonabant, as described above. Differential scanning fluorimetry assays were performed in 96-well PCR plates using a real-time PCR machine (CFX96, Bio-Rad). Standard assay conditions (25 μl) were 25 mM HEPES pH 7.5, 150 mM NaCl, 0.01% LMNG, 0.002% CHS and 10 μM of the corresponding ligands. The protein concentration was 2 μM and the BODIPY FL-L-cystine dye<sup>38</sup> was added at 2 μM final concentration. All reactions were incubated at 4 °C for 20 min before scanning in the PCR machine. The fluorescence was measured at 0.5 °C temperature intervals from 4 °C to 90 °C by using the FAM filter set (450–490 nm excitation, 515–530 nm emission).

**Crystallization.** Purified receptor was concentrated to 55 mg ml<sup>-1</sup> using a 100-kDa cut-off Vivaspin column (Sartorius), and crystallized using the LCP method. The concentrated receptor was reconstituted into a lipid mixture containing monolein plus 10% (w/w) cholesterol (Sigma), at a ratio of 2:3 receptor to lipid (by weight). Mixing was performed at room temperature using a syringe mixing apparatus as previously described<sup>39</sup>. The mesophase was dispensed in 40-nl drops onto 96-well glass plates and overlaid with 800 nl precipitant solution using a Gryphon LCP robot (Art Robbins Instruments). Crystals grew to full size after 2 weeks at 20 °C in the following overlay precipitant condition: 31% PEG 400, 100 mM sodium citrate pH 5.5, 100 mM magnesium sulfate. The crystals were harvested from LCP setups using MiTeGen loops and cryoprotected in liquid nitrogen.

**Data collection and processing.** X-ray diffraction data were collected at GM/CA-CAT beamline 23ID-B at the Advanced Photon Source (APS), Argonne National Laboratory, equipped with an Eiger 16M detector. Datasets were acquired using a beam size of 20 μm with 1.033-Å wavelength X-rays. For each crystal, fifty 0.4° oscillation images were collected, with 1-s exposure and without attenuation of the beam. Owing to radiation damage of crystals, a 97% complete diffraction data was merged from 42 crystals and scaled using HKL3000<sup>40</sup>. The dataset was

processed in space group *P*2<sub>1</sub>, and a resolution cut-off of 2.6 Å was selected by examining CC<sub>1/2</sub> values after anisotropy correction in HKL3000.

**Structure determination and refinement.** The structure of CB1(T210A)–PGS in complex with taranabant was solved by molecular replacement with Phaser<sup>41</sup> using human S1P<sub>1</sub> receptor<sup>19</sup> (PDB: 3V2Y) and PGS<sup>42</sup> (PDB: 2BFW) as independent search models. The solution was improved through iterations of manual building in Coot<sup>43</sup>, followed by refinement using Refmac5 (ref. 44). Translation-libration-screw refinement was used to model atomic displacement factors. Refinement parameters for the taranabant ligand were generated using the PRODRG<sup>45</sup> web server. The resulting statistics for data collection and refinement are included in Extended Data Table 1. The final structure had 96.6% of residues in the favoured region of the Ramachandran plot, 3.4% in the allowed region, and 0 residues disallowed. Figures were prepared using PyMol (Schrodinger LLC). The electrostatic potential surface shown in Fig. 1c was calculated using APBS<sup>46</sup>.

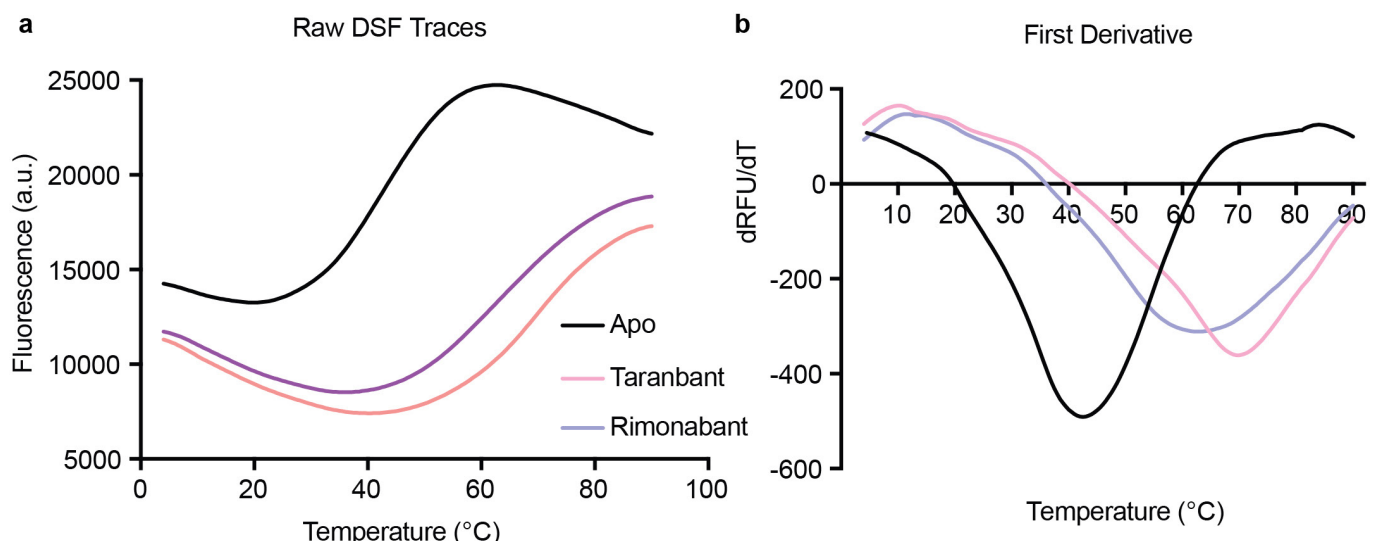
**Binding of ligands to the CB1 receptor.** Ligand-binding experiments on membranes containing CB1 wild-type, CB1–PGS, and CB1(T210A)–PGS were carried out based on a previously published protocol<sup>28</sup>. Sf9 cells expressing each construct (without any ligand present) were used to generate membranes by Dounce homogenization and differential centrifugation<sup>18</sup>. Saturation binding was carried out by incubating 1.5–5 μg of membranes with different concentrations of [<sup>3</sup>H]SR141716A (54 Ci mmol<sup>-1</sup>; Perkin-Elmer) between 0.05 and 25.6 nM in assay buffer (25 mM Tris pH 7.5, 5 mM MgCl<sub>2</sub>, 1 mM EDTA) containing 0.1% protease-free BSA in a final volume of 250 μl per tube. Reactions were incubated at 30 °C for 1 h and then quenched with 250 μl assay buffer with 5% BSA. Non-specific binding was determined using reactions containing 1 μM unlabelled ligand. Reactions were separated on a vacuum manifold using GF/C filters (pre-soaked in assay buffer supplemented with 0.5% polyethylenimine) to retain membranes and discard unbound ligand. After washing four times with cold assay buffer, bound radioactivity was quantified using a scintillation counter. For competition-binding experiments, aliquots of membranes were incubated with 3 nM [<sup>3</sup>H]SR141716A, and varying concentrations of competitor ligands (taranabant or CP55940) were included in the binding reactions. All binding experiments were carried out as three independent experiments, each performed in duplicate. Data analysis and fitting was performed with GraphPad Prism (GraphPad Software Inc.).

**Molecular dynamics simulations.** The system used for molecular dynamics simulation consisted of one copy of CB1 receptor (PGS domain removed), taranabant, 240 POPC (1-palmitoyl-2-oleoyl-sn-glycero-3-phosphocholine) molecules, 48 Na<sup>+</sup>, 57 Cl<sup>-</sup>, and 17,087 water molecules. Molecular dynamics simulations were performed with periodic boundary condition to produce isothermal-isobaric ensembles using the modified PMEMD.CUDA program in AMBER 14 (ref. 47). Temperature was regulated using Langevin dynamics<sup>48</sup> with a collision frequency of 5 ps<sup>-1</sup>. Pressure was regulated using the isotropic position scaling algorithm with the pressure relaxation time set to 1.0 ps. The integration of the equations of motion was conducted at a time step of 1 fs for the relaxation phase and 2 fs for the equilibrium and sampling phases. After a 5-ns equilibration, a 55-ns molecular dynamics simulation was performed at 298 K, 1 bar to produce constant temperature and pressure ensembles. The transmembrane helices were very stable in both simulations and the mean r.m.s.d. values were  $1.52 \pm 0.13$  and  $1.45 \pm 0.23$  Å for the apo and complex forms, respectively. The r.m.s.d. values of the membrane-proximal N-terminal region of the complex form ( $0.96 \pm 0.24$  Å) were smaller than those of the apo form ( $1.28 \pm 0.19$  Å).

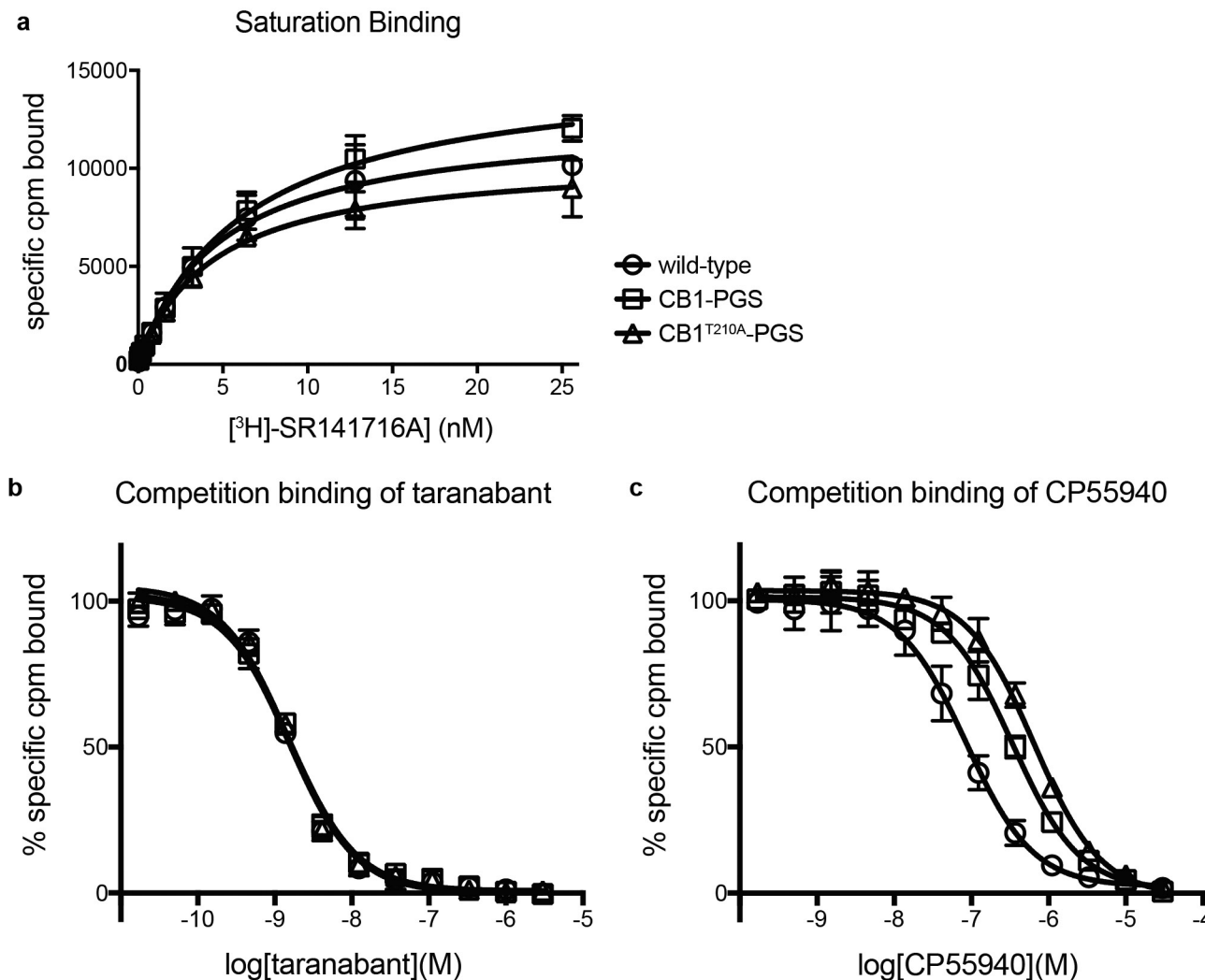
**Docking of rimonabant and THC.** Molecular docking was performed for taranabant, rimonabant, and THC using Glide<sup>49,50</sup>, implemented in the Schrodinger software package (<http://www.schrodinger.com>). Different protocols of receptor preparation, grid generation and flexible ligand docking were evaluated and the one that produced the best docking scores was adopted. The optimal Glide protocol for CB1 included: only optimize hydrogen atoms in the receptor preparation; allow hydroxyl and thiol groups of Thr197, Ser383 and Cys386 to be rotatable; use the standard precision scoring function. We first tested our docking protocol by re-docking the taranabant ligand from the crystal structure. The best docking scores were –12.76 and –12.59 kcal mol<sup>-1</sup> for the crystal conformation and a 3D conformation generated without any initial bias using the Concord program (<http://www.certara.com>), respectively. The r.m.s.d. between the crystal structure and docking pose was 0.55 Å for the Concord conformation. Next, the antagonist rimonabant and the partial agonist THC were docked to the binding pocket using the same protocol. The docking scores of the best docking poses were –8.99 and –9.36 kcal mol<sup>-1</sup> for rimonabant and THC, respectively.

**Data availability.** Atomic coordinates and structure factors for the reported crystal structure have been deposited in the Protein Data Bank (PDB) under the accession code 5U09. All other data are available from the corresponding author upon reasonable request.

38. Hofmann, L., Gulati, S., Sears, A., Stewart, P. L. & Palczewski, K. An effective thiol-reactive probe for differential scanning fluorimetry with a standard real-time polymerase chain reaction device. *Anal. Biochem.* **499**, 63–65 (2016).
39. Caffrey, M. & Cherezov, V. Crystallizing membrane proteins using lipidic mesophases. *Nat. Protocols* **4**, 706–731 (2009).
40. Otwinowski, Z. & Minor, W. Processing of X-ray data collected in oscillation mode. *Methods Enzymol.* **276**, 307–326 (1997).
41. McCoy, A. J. et al. Phaser crystallographic software. *J. Appl. Crystallogr.* **40**, 658–674 (2007).
42. Horcajada, C., Guinovart, J. J., Fita, I. & Ferrer, J. C. Crystal structure of an archaeal glycogen synthase: insights into oligomerization and substrate binding of eukaryotic glycogen synthases. *J. Biol. Chem.* **281**, 2923–2931 (2006).
43. Emsley, P., Lohkamp, B., Scott, W. G. & Cowtan, K. Features and development of Coot. *Acta Crystallogr. D* **66**, 486–501 (2010).
44. Skubák, P., Murshudov, G. N. & Pannu, N. S. Direct incorporation of experimental phase information in model refinement. *Acta Crystallogr. D* **60**, 2196–2201 (2004).
45. Schüttelkopf, A. W. & van Aalten, D. M. F. PRODRG: a tool for high-throughput crystallography of protein-ligand complexes. *Acta Crystallogr. D* **60**, 1355–1363 (2004).
46. Baker, N. A., Sept, D., Joseph, S., Holst, M. J. & McCammon, J. A. Electrostatics of nanosystems: application to microtubules and the ribosome. *Proc. Natl Acad. Sci. USA* **98**, 10037–10041 (2001).
47. Case, D. A. et al. The Amber biomolecular simulation programs. *J. Comput. Chem.* **26**, 1668–1688 (2005).
48. Izaguirre, J. A., Catarello, D. P., Wozniak, J. M. & Skeel, R. D. Langevin stabilization of molecular dynamics. *J. Chem. Phys.* **114**, 2090–2098 (2001).
49. Friesner, R. A. et al. Glide: a new approach for rapid, accurate docking and scoring. 1. Method and assessment of docking accuracy. *J. Med. Chem.* **47**, 1739–1749 (2004).
50. Friesner, R. A. et al. Extra precision glide: docking and scoring incorporating a model of hydrophobic enclosure for protein-ligand complexes. *J. Med. Chem.* **49**, 6177–6196 (2006).

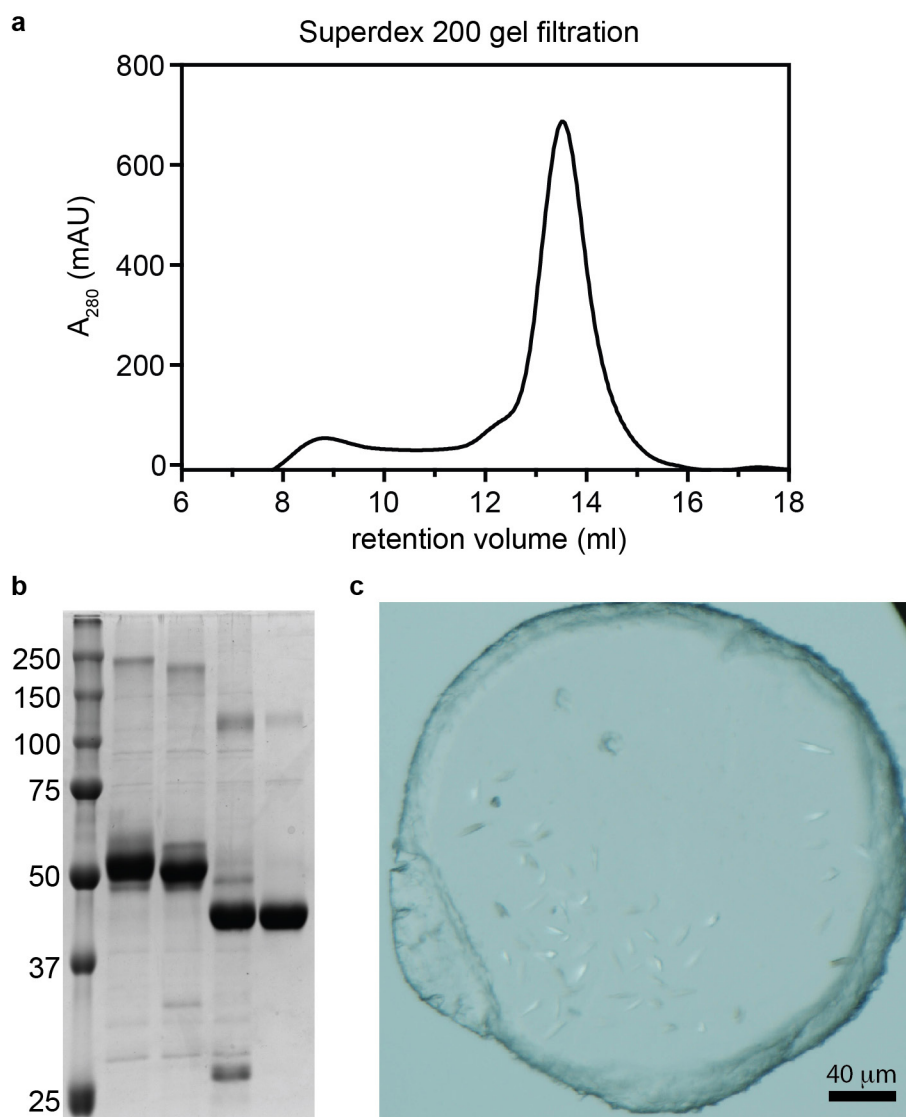


**Extended Data Figure 1 | Differential scanning fluorimetry on purified CB1-PGS.** **a**, Raw differential scanning fluorimetry traces of the receptor in the apo state or bound to each antagonist. **b**, First derivative analysis of data in **a**.



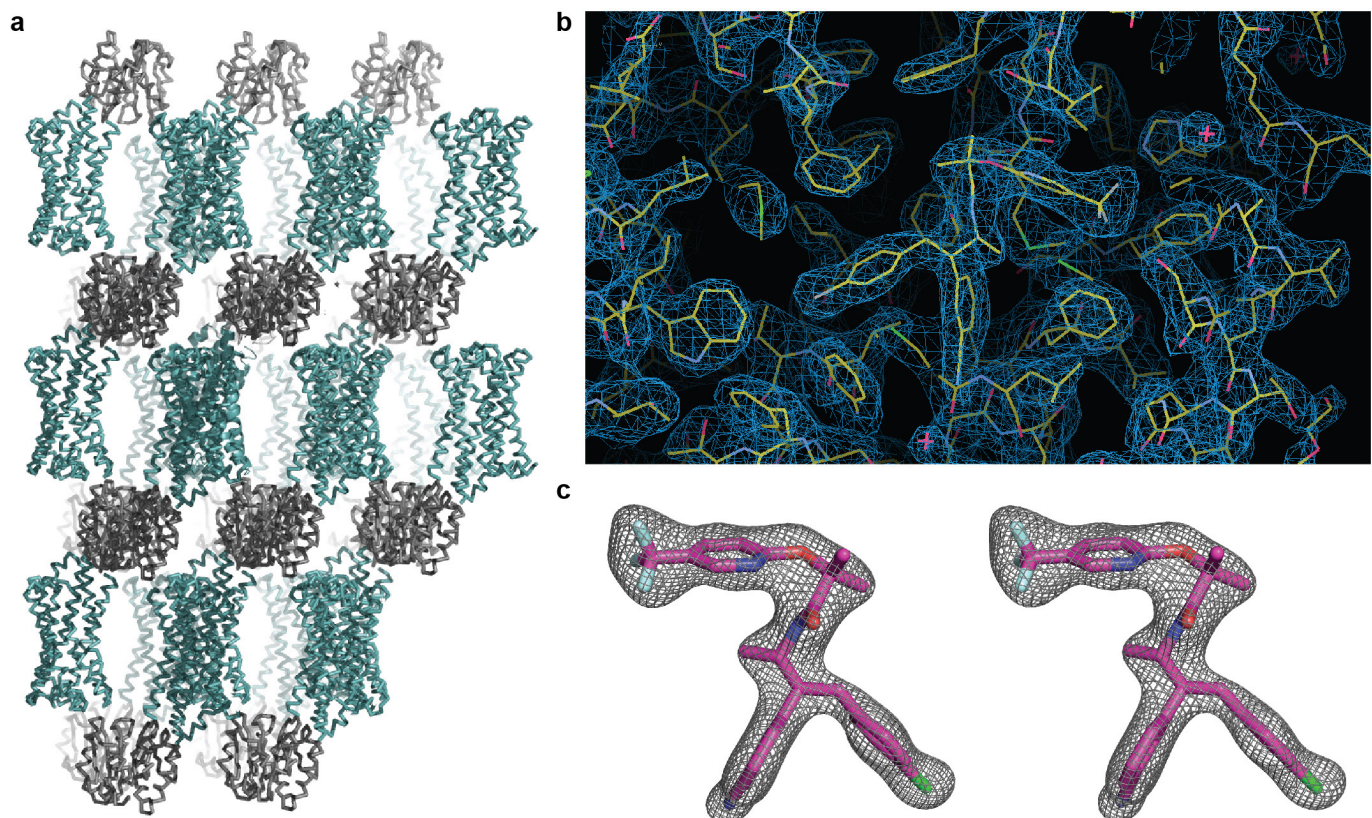
**Extended Data Figure 2 | Ligand-binding properties of CB1 constructs.**  
**a**, Saturation binding of the antagonist [ $^3\text{H}$ ]SR141716A (tritiated rimonabant radioligand) to wild-type CB1, CB1-PGS, and CB1(T210A)-PGS. Error bars represent s.d. for three separate experiments, each performed in duplicate. The fitted  $K_d$  values ( $\pm$  s.e.m.) for these three constructs are  $4.8 \pm 0.7$  nM,  $6.3 \pm 0.6$  nM, and  $4.4 \pm 0.5$  nM, respectively.  
**b**, Competition binding of taranabant to the wild-type CB1 receptor, CB1-PGS, and CB1(T210A)-PGS. Error bars represent s.d. for three

separate experiments, each performed in duplicate. The  $K_i$  values ( $\pm$  s.e.m.) of the three constructs for taranabant are  $0.94 \pm 0.17$  nM,  $1.10 \pm 0.16$  nM, and  $0.91 \pm 0.16$  nM, respectively. **c**, Competition binding of the agonist CP55940 to the wild-type CB1 receptor, CB1-PGS, and CB1(T210A)-PGS. Error bars represent s.d. for three separate experiments, each performed in duplicate. The  $K_i$  values ( $\pm$  s.e.m.) of the three constructs for CP55940 are  $53 \pm 12$  nM,  $230 \pm 43$  nM, and  $384 \pm 62$  nM, respectively.



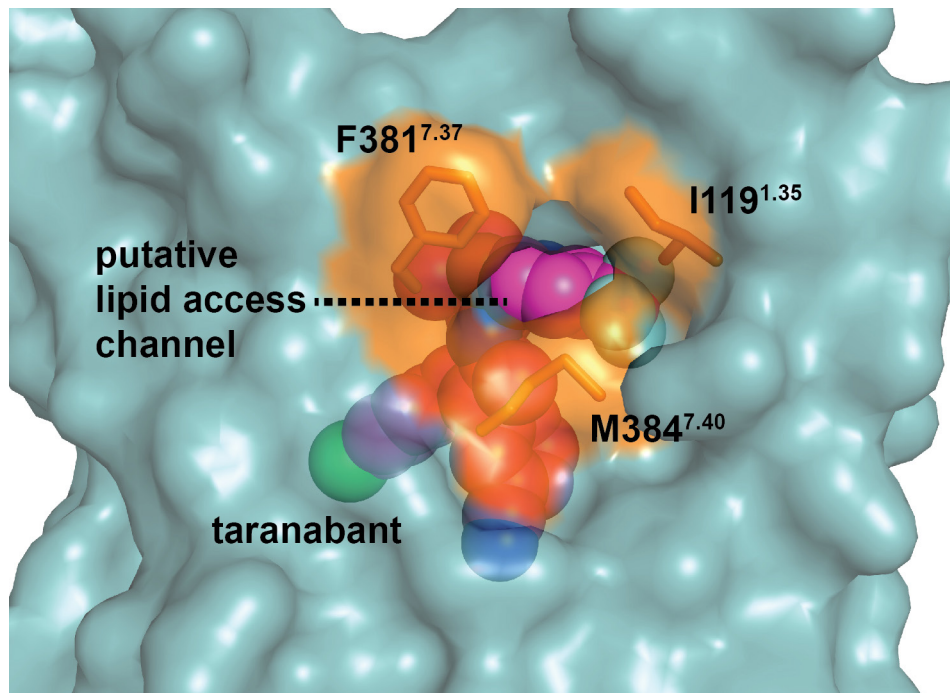
**Extended Data Figure 3 | Purification and crystallization of CB1(T210A)-PGS.** **a**, Superdex 200 gel-filtration trace of receptor after Ni immobilized metal-affinity chromatography (IMAC) and M1 anti-Flag chromatography (see Methods). **b**, SDS-PAGE analysis of samples at different stages of purification. The five lanes from left to right are:

markers (molecular mass in kDa at left); IMAC/Flag-purified receptor; same sample after treatment with PNGaseF; receptor after TEV protease cleavage (removing 89 N-terminal amino acids); final sample after Superdex 200 gel filtration. **c**, Light microscopy image showing examples of LCP microcrystals of CB1(T210A)-PGS used to collect diffraction data.



**Extended Data Figure 4 | Packing and electron density in the CB1(T210A)-PGS crystals.** **a**, Lattice packing interactions in the monoclinic crystals of CB1(T210A)-PGS. Protomers are shown as ribbons, with the receptor component of the fusion protein coloured teal and the PGS domain coloured grey. **b**,  $2F_o - F_c$  electron density map

(contoured at  $1.2\sigma$ ) of taranabant and the surrounding ligand-binding residues. Protein and ligand are represented as yellow sticks. **c**, Stereo view of  $2F_o - F_c$  electron density (contoured at  $1.5\sigma$ ) for only the ligand taranabant (magenta sticks).

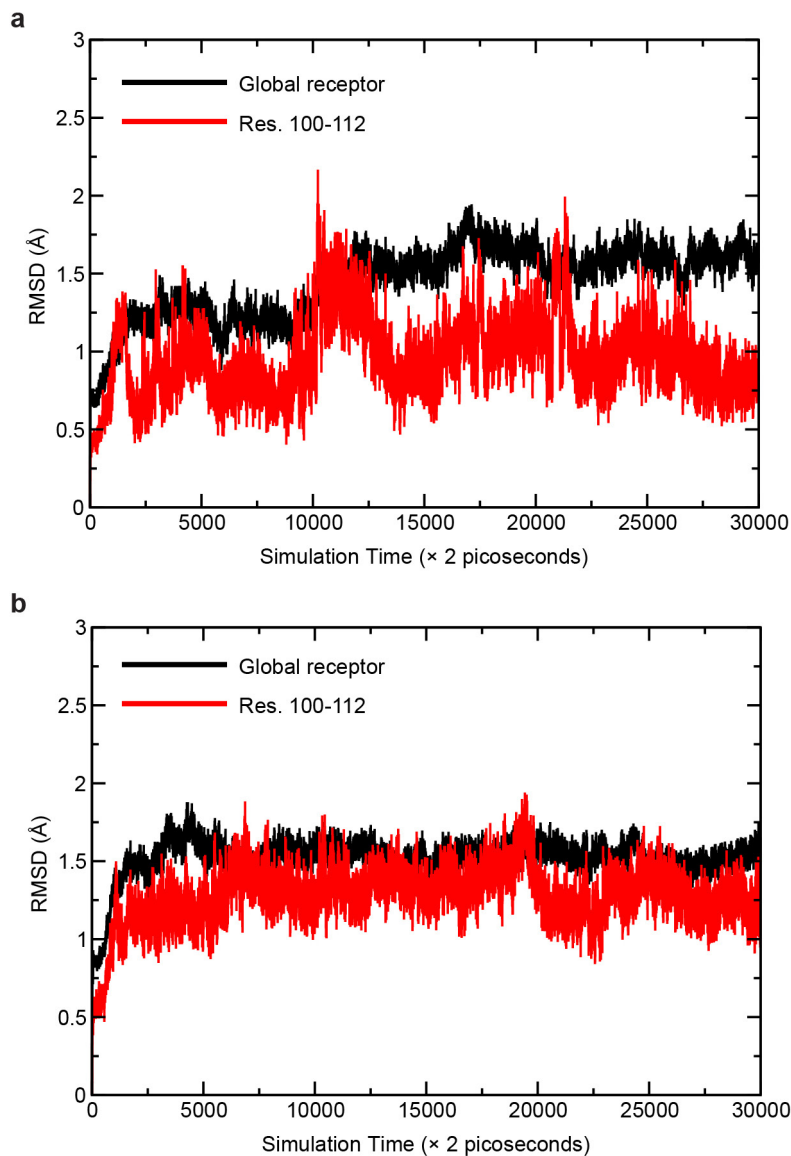


**Extended Data Figure 5 | Residues lining the putative lipid access channel of CB1.** The receptor is shown as a teal transparent surface, and taranabant is in magenta spheres. The three residues lining the channel are shown as orange sticks and their solvent-accessible surfaces are coloured orange.

Human	90	KENEENIQCGENFMDIECFMVLN	112
Horse	90	KENEENIQCGENFMDMECFMILN	112
Bovine	90	KENDENIQCGENFMDMECFMILN	112
Cat	90	KENEENIQCGENFMDMECFMILN	112
Mouse	91	KENEDNIQCGENFMDMECFMILN	113
Chicken	92	KENEENIQCGENFMDMECFMILN	114
Frog	90	KDTDDNVQCGKNFMDMECFMILT	112
Zebrafish	98	HAEDGSLQCGENFMDMECFMILT	120

**Extended Data Figure 6 | Sequence alignment of the membrane-proximal N-terminal region of CB1 from different vertebrate species.** ‘Frog’ is *Xenopus laevis*. The red bar (top) indicates the part of this region that is structured and visible in the electron density of the CB1 crystals.

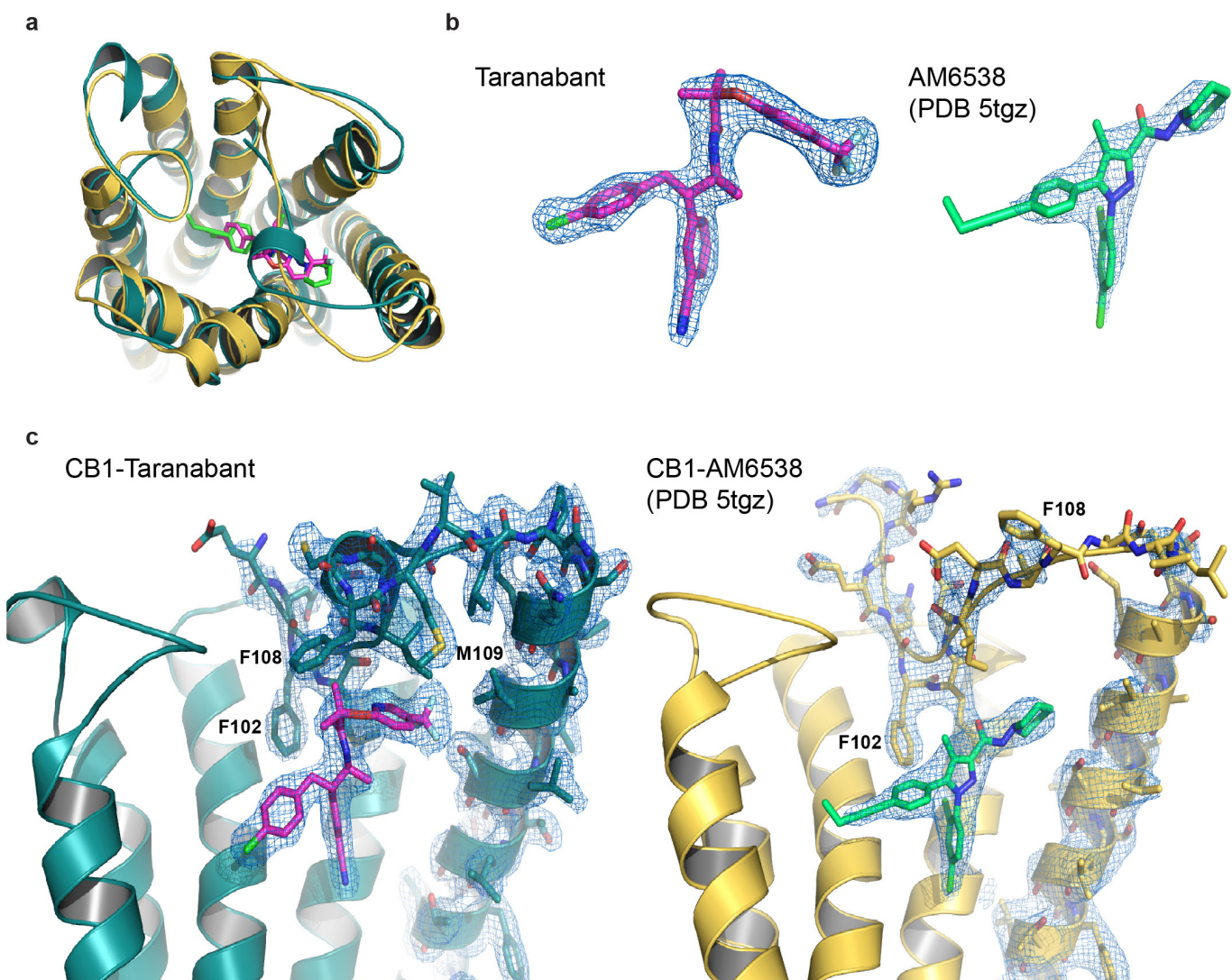
The blue box denotes positions that make contact with taranabant. Alignment was performed using Clustal Omega (<https://www.ebi.ac.uk/Tools/msa/clustalo/>).



**Extended Data Figure 7 | Molecular dynamics simulation of the CB1 structure.** **a**, A 60-ns molecular dynamics simulation of the CB1 receptor (after removing the PGS fusion protein) with taranabant present. Black trace is for the entire receptor, red trace is for only the structured membrane-proximal N-terminal region. **b**, 60-ns molecular dynamics simulation of the CB1 receptor without a ligand present. Black trace is for the entire receptor, red trace is for only the structured membrane-proximal N-terminal region.

membrane-proximal N-terminal region. **b**, 60-ns molecular dynamics simulation of the CB1 receptor without a ligand present. Black trace is for the entire receptor, red trace is for only the structured membrane-proximal N-terminal region.

**Extended Data Figure 8 | Sequence alignment of the entire sequence of CB1 from several different species, along with human CB2.** The blue boxes denote positions that make contact with taranabant within a 4 Å cut-off. The alignment was performed using Clustal Omega (<https://www.ebi.ac.uk/Tools/msa/clustalo/>).



**Extended Data Figure 9 | Comparison of the structures of CB1 bound to taranabant and CB1 bound to AM6538 (ref. 34; PDB accession 5TGZ).**  
**a**, Superposition of the two CB1 structures viewed from the extracellular space. The taranabant-bound structure is shown as a teal cartoon (ligand as magenta sticks), while the AM6538-bound structure is shown as a gold cartoon (ligand as green sticks). **b**, Comparison of  $2F_o - F_c$  electron density (contoured at  $1.5\sigma$ ) for the ligands in each structure. On the left is

taranabant from the current structure, on the right is AM6538 from ref. 34. **c**, Comparison of the membrane-proximal N-terminal regions in each structure. On the left is a side view of CB1 from the current structure, with  $2F_o - F_c$  electron density (contoured at  $1.0\sigma$ ) shown for the N-terminal region, TM1, and taranabant. On the right is the analogous side view of CB1 from ref. 34 (gold cartoon), with  $2F_o - F_c$  electron density (contoured at  $1.0\sigma$ ) shown for the N-terminal region, TM1 and AM6538.

Extended Data Table 1 | Data collection and refinement statistics

CB1-PGS with Taranabant <sup>¶</sup>	
<b>Data collection</b>	
Space group	P2 <sub>1</sub>
Cell dimensions	
<i>a, b, c</i> (Å)	50.7, 80.4, 81.2
$\beta$ (°)	91.7
Resolution (Å)	50.00-2.60 (2.69-2.60) <sup>†</sup>
$R_{\text{sym}}$ or $R_{\text{merge}}$ <sup>‡</sup>	0.19 (NA)
$I/\sigma I$	7.43 (0.96)
Completeness (%)	96.8 (96.9)
Redundancy	5.4 (5.1)
CC <sub>1/2</sub> in highest shell	0.69
<b>Refinement</b>	
Resolution (Å)	50-2.60
No. reflections	11084
$R_{\text{work}} / R_{\text{free}}$	0.19 / 0.23
No. atoms	
Protein	3762
Ligand/ion	56
Other (Lipid and water)	125
B-factors	
Receptor	45.5
Fusion protein	38.3
Ligand	42.0
Ion	91.0
Other (Lipid and water)	44.4
R.m.s deviations	
Bond lengths (Å)	0.008
Bond angles (°)	1.20

<sup>¶</sup>Diffracton data from 42 crystals were merged into a single dataset.<sup>†</sup>Values in parentheses are for the highest-resolution shell.<sup>‡</sup> $R_{\text{merge}} > 1$  is statistically meaningless, Scalepack<sup>40</sup> does not report it.